PHYSICAL REVIEW C VOLUME 26, NUMBER 4 OCTOBER 1982

Inelastic electron scattering from ^{3}He and ^{4}He in the threshold region at high momentum transfer

S. Rock, R. G. Arnold, B. T. Chertok,* and Z. M. Szalata
American University, Washington, D.C. 20016

D. Day and J. S. McCarthy
University of Virginia, Charlottesville, Virginia 22901

F. Martin
Stanford Linear Accelerator Center, Stanford, California 94305

B. A. Mecking
Universität Bonn, Bonn, West Germany

I. Sick
Universität Basel, Basel, Switzerland

G. Tamas
Center d'Etudes Nucléaires de Saclay, Gif-sur-Yvette, France
(Received 19 February 1982)

The cross section for inclusive inelastic electron scattering from the helium isotopes has been measured at momentum transfers squared of $0.8 \le Q^2 \le 5.0$ (GeV/c)^2 for ^{3}He and $0.8 \le Q^2 \le 2.4$ (GeV/c)^2 for ^{4}He. The data were taken at 8° and cover the range $0.6 < x < 1$, where $x = Q^2/2M_{\text{He}}\nu$, which includes the elastic peak, nuclear breakup threshold, the high momentum tail of the quasielastic scattering, and pion production. The structure function, νW_2, derived from the data, is approaching a scaling limit at high Q^2. It can be factored into a product of functions of Q^2 and of x as predicted by some models.

[NUCLEAR REACTIONS ^{3}He, ^{4}He$(e,e')X$; $E = 6.4-16.5$ GeV; $\theta_e = 8°$; measured $d\sigma/d\Omega\, dE'$; deduced νW_2 at threshold.]

I. INTRODUCTION

In this experiment we measured the inclusive inelastic cross section of electrons scattered from ^{3}He and ^{4}He, $e-\text{He} \rightarrow e'-X$, near the exclusive elastic limit. Data for ^{3}He (^{4}He) were taken at 12 (7) values of the momentum transfer squared (Q^2) in the range 0.8–5.0 (0.8–2.4) (GeV/c)^2 in conjunction with a measurement of the elastic scattering cross section.[1]

The final state hadron had a mass of up to 200 MeV above the mass of the initial nucleus. This region can be interpreted as the extreme tail of quasielastic scattering from the nucleons within the nucleus. Scattering near threshold can also be looked at as an extension of elastic scattering. For example, the Drell-Yan and West model[2] of the nucleon predicts that both the elastic and threshold inelastic cross sections depend on scattering from one constituent within the bound state which carries almost all of the longitudinal momentum. Parton model analyses using infinite momentum frame techniques were applied to the large Q^2 inelastic electron scattering from nuclei.[3,4] Brodsky and Chertok[3] treat the threshold scattering as a sum of elastic scattering from the individual nucleons within the nucleus with the application of quark-counting rules to account for residual nuclear interactions (Fermi motion). Schmidt and Blankenbecler[4] discuss a more general situation by considering the elastic scattering from all possible constituents or clusters of constituents moving within the nucleus as the mechanism for threshold inelastic scattering. A dispersion theory approach using similar ideas was developed by Frankfurt and Strikman.[5] They have also calculated[6] the high momentum tail of the nuclear wave function within perturbative quantum chromodynamics (QCD) and the effects of few nucleon correlations on threshold $e+{}^3\text{He}\rightarrow e'+X$.

The scaling behavior of the $e-p$ inelastic structure function is due to elastic scattering from the quark constituents of the proton. Similarly, a study of scaling of the $e-d$ structure function[7] at high Q^2 near threshold and the ^{3}He and ^{4}He structure functions presented below can yield information on whether the nucleus is in a multiquark state.

The experiment was performed at the Stanford Linear Accelerator Center (SLAC) using high pressure helium gas targets and the facilities of End Station A. The running conditions were optimized for the elastic scattering measurement in which the scattered electrons were detected in the 20 GeV spectrometer in coincidence with the recoil nuclei detected in the 8 GeV spectrometer. In this paper we present the single-arm 20 GeV spectrometer inclusive electron data taken simultaneously with the elastic scattering data.

The rest of this paper is organized as follows: The experimental apparatus is described in Sec. II; calibration and analysis are discussed in Sec. III. Section IV contains the results and conclusions.

II. APPARATUS

A. Overview

The experimental layout is shown in Fig. 1. Electrons from the accelerator passed through energy defining slits and charge monitors and then struck a high pressure He gas target. Scattered particles were identified and their momentum and angle determined by scintillation and shower counters and proportional wire chambers in the 20 GeV spectrometer. A more detailed description of the apparatus can be found in the rest of this section and in Ref. 8.

B. Beam

The average beam current was set between 0.1 and 11 μA depending on the target and momentum transfer being studied. The maximum instantaneous current was 45 mA during the 1.5 μsec SLAC spill. The total charge in the beam was measured by two separate toroids which agreed to better than 2% at all times. The toroids were calibrated aganist a Faraday cup several times during the experiment.

The energy defining slits were adjusted so as to allow maximum beam current at high Q^2 and good resolution at low Q^2. The slits varied from 0.2% to 0.6% full width in $\Delta E/E$.

C. Target

High-pressure, low-temperature gas targets were used. The gaseous helium was circulated through a heat exchanger cooled with liquid hydrogen to dissipate the heat deposited by the electron beam. Two 41-cm-long target cells were used, one at 50 atm and the other at 10 atm filled with either ^{3}He or ^{4}He. These cells were matched to the needs of the elastic scattering experiment where lower density was required at low Q^2 to allow measurement of slow recoiling nuclei. Table I gives details of the He targets. The target density was determined from calibrated temperature and pressure sensors and the National Bureau of Standards density tables[9] with an estimated error of ±3%. Over 2000 l at standard temperature and pressure (STP) gas consisting of 98.15% ^{3}He and 1.8% ^{4}He were in the system. A series of rate measurements at various beam currents up to the maximum of 15 μA average current indicated that the target system could dissipate the approximately 150 W of energy deposited with at most a 3% decrease in target density.

The target system also included a 60-cm-long

TABLE I. Some properties of the He target cells and the He gas. Each cell could be filled with either ^{3}He or ^{4}He. The low pressure cell was used at low Q^2 and the high pressure cell at large Q^2 as indicated in the last column.

Cell	Length (cm)	Pressure (atm)	Temp (deg K)	End caps Al (cm)	Density ^{3}He (g/cm)^3	Density ^{4}He (g/cm)^3	Q^2 (GeV/c)^2
Low pressure	41.6	10	21	0.0094	0.0165 ±3%	0.0234 ±3%	0.8, 1.0
High pressure	41.8	50	21	0.041	0.068 ±3%	0.095 ±3%	>1.0

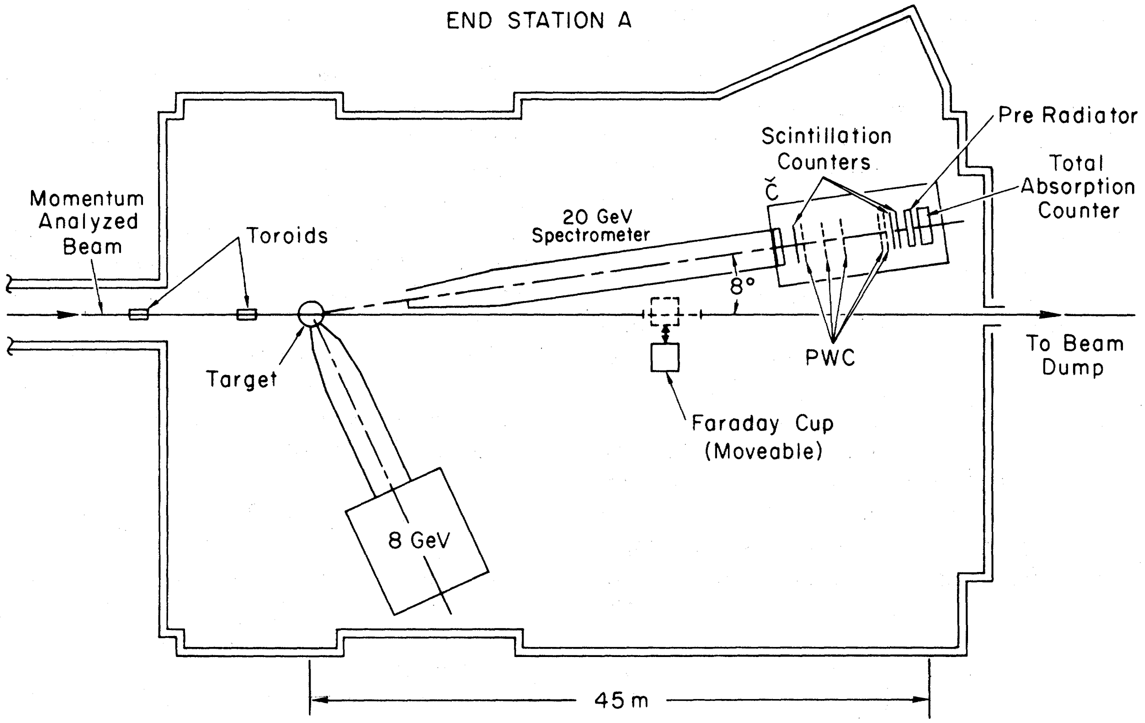

FIG. 1. Experimental setup showing the 20 GeV spectrometer set at 8°. The 8 GeV spectrometer was not used for these inelastic measurements.

liquid hydrogen target used for system calibration and an empty target with 2.2-mm-thick Al end cap windows. These were 24.0 and 5.6 times thicker than the Al end cap windows of the high and low pressure He cells, respectively. The enhanced thickness was used to match the radiation lengths of the full and empty cells (to within 5% for the high pressure target) and to speed up the empty cell data taking. The Al windows of the He cells represented 8% (5%) of the integrated density of the ^{3}He and (^{4}He). All targets were remotely positioned from the experimental control station. Further details of the target can be found in Ref. 8.

D. Spectrometer

The scattered electrons which were transported through the spectrometer were identified and measured by three plastic scintillation counters, a total absorption counter, a nitrogen gas Čerenkov counter, and five planes of proportional wire chambers. The trigger used to record an event consisted of a coincidence between signals from the three scintillation counters and a large pulse-height signal in the total absorbtion counter.

The 20 GeV spectrometer[10] is a 50-m-long system of eleven magnets which transports particles from the target to momentum and production angle focusing planes. It has a nominal acceptance of $\Delta p/p=\pm 2\%$ in momentum, ± 8 mrad in the azimuthal angle ϕ, ± 4.5 mrad in the polar scattering angle θ, and ± 3 cm in projected target length. The actual shape of the acceptance phase volume averaged over target length is a complicated function determined by many elements of the system.

Since the cross section is a function of θ and p only, we are interested in finding the ϕ acceptance of the spectrometer at each value of θ and p within the $\theta-p$ acceptance. This ϕ acceptance was obtained using a Monte Carlo ray trace model of the target-spectrometer-detector system. In the momentum interval $-2\% < \Delta p/p < 2\%$ and angle interval -4 mrad $< \Delta\theta < 3$ mrad, the ϕ acceptance varies from 16 mrad at the center to approximately 10 mrad at the edges.

To optimize the elastic scattering rate, the elastic scattering peaks were placed in the center of the 20 GeV spectrometer momentum acceptance. At each value of Q^2 selected for the elastic scattering measurement, the inelastic data were collected at a single angle (θ_c) and momentum ($p_{\rm el}$) setting of the spectrometer. Thus, the inelastic scattering data populates only that half of the momentum acceptance which extends from $p_{\rm el}$ to the edge of

$$\Delta p=(p_{\mathrm{el}}-p)/p_{\mathrm{el}}=-0.02 \ .$$

Based on the results of the proton calibration and resolution studies (Secs. III A and D), we estimate uncertainly of the ϕ acceptance to be 4% in this region.

The transport coefficients[11] which relate the measured positions of the particles in the wire chamber detectors to the angles and momenta at the target were obtained by a fit to the 1967 optics measurements. Comparisons with an independently determined set of transport coefficients,[12] and with acceptance tests made in 1979, indicate an uncertainty of up to 0.1% in $\Delta p/p$ and 0.25 mrad in $\Delta\theta$.

III. ANALYSIS AND CALIBRATION

A. Proton calibration

Throughout the experiment elastic proton data were taken periodically to calibrate the entire system for both energy resolution and spectrometer acceptance. Since the $e-p$ elastic scattering cross section is approximately five orders of magnitude greater then the $e-$He elastic cross section, it is ideal for rapid calibration. These data were taken at a variety of incident energies, beam intensities, and counting rates with the elastic peak centrally located in the spectrometer momentum acceptance. Including the smearing due to finite resolution and the radiative tail, the elastic events filled that half of the momentum acceptance which extends from $\Delta p/p=0.1\%$ to -2%. The width of the elastic peak measures the resolution of the system. The reconstructed mass of the elastic peak provides the energy-angle calibration of the beam-spectrometer system. The magnitude of the cross section obtained compared to the world average cross section tests the acceptance near the center of the spectrometer, charge monitors, target density, wire chamber efficiency, dead time corrections, and analysis procedures.

The calibration analysis was done by two methods. In both cases data were sorted into missing mass squared W^2 (0.02 GeV^2) and angle θ (0.4 mrad) bins. The cross section was obtained in each bin by using the acceptance of that bin determined from the Monte Carlo model.

In the first method, the elastic cross section at each θ bin value was obtained by integrating over the range of W^2 from 0.84 to 1.08 GeV^2. This includes the elastic peak and a portion of the radiative tail. The experimental cross sections for each bin of θ were corrected for radiative effects using

$$\left.\frac{d\sigma}{d\Omega}\right|_{\mathrm{final}}=\left.\frac{d\sigma}{d\Omega}\right|_{\mathrm{exp}} e^{\delta(\Delta E)} \ , \tag{3.1}$$

where $\delta(\Delta E)$ is determined from the formulas of Mo and Tsai[13] and $\Delta E=E'$ (elastic) $-E'$ (cutoff). The cross section varied by approximately 50% over the θ acceptance of the spectrometer. Approximately 20% of the variation was due to the Mott factor and the rest due to the structure functions. The elastic cross sections at each bin of θ, ranging from -4 to $+3$ mrad from the central value of 8°, were divided by the cross sections from the Iachello, Jackson, and Lande (IJL) Ref. 14 fit to the World Data at the same kinematic conditions. These ratios of cross sections were then averaged over θ and the results are shown in Fig. 2.

The second method is almost identical to that used for the inclusive He analysis (discussed in Sec. III B). At each bin of W^2, the cross sections $d\sigma/d\theta\, dW^2$ were fitted by a polynomial in θ and the value of $d\sigma/dW^2$ was obtained at $\theta=8°$. This cross section was then integrated over W^2 and radiatively corrected using Eq. (3.1).

The results of method I averaged over all 16 runs gives $\sigma(\mathrm{US})/\sigma(\mathrm{world})=0.995\pm0.004$ and method II gives 0.954 ± 0.007, where the errors come from counting statistics only. The scatter of values in Fig. 2 indicates a fluctuating systematic error of ap-

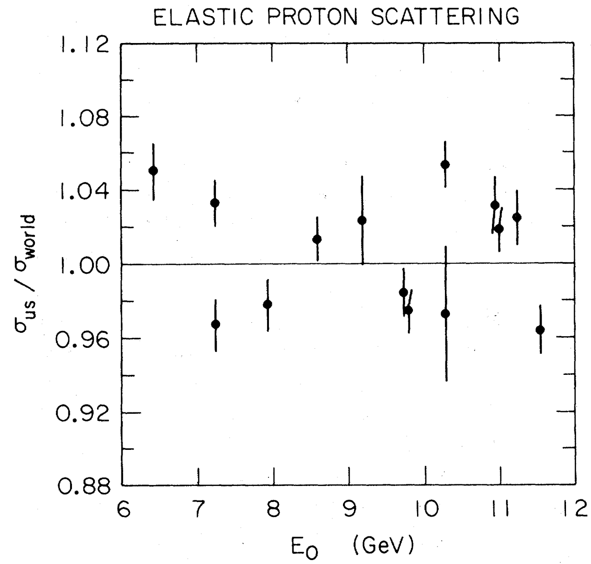

FIG. 2. Elastic proton scattering calibration. The ratio between our elastic proton cross sections and a fit to the previous world data by IJL (Ref. 11) is plotted as a function of incident energy. Errors are statistical only.

TABLE II. The sources and estimated values of the systematic errors.

Target density	3%
Resolution	2–15 %
Energy calibration	4–12 %
Solid angle	4%
Incident charge	2%
Radiative corrections	4%
^{4}He contamination	2%

proximately $2\frac{1}{2}$% from run to run. The agreement with World Data is better than expected from the estimates of the relevant systematic uncertainties shown in Table II. These are uncertainties in the target density, incident charge, and acceptance near the center of the spectrometer. The difference between the methods reflects some of the uncertainties in the analysis procedures.

B. He analysis

The criteria for good electron events were that they had reconstructable tracks in the wire chambers and large pulse heights in the shower counter. The fraction of triggers producing reconstructable tracks varied between 80% at high Q^2 and 90% at low Q^2 and depended on the rate of background in the detectors. For $Q^2 < 2$ (GeV/c)^2, more than 99% of the candidates passed the shower pulse height criterion. The fraction declined to 30% at $Q^2=4$ (GeV/c)^2. The electron-hadron separation using the shower counter at $Q^2=4$ (GeV/c)^2 is shown in Fig. 3. The results from the Čerenkov counter corroborated the event selection criteria.

To obtain spectra of inelastic e-He events, it is necessary to subtract the background of elastically scattered electrons and the background of electrons scattered in the target end caps. These backgrounds are discussed in Sec. III C.

Good electron events from the full target, the end caps, and elastic scattering were binned in separate two-dimensional histograms in scattered momentum ($\Delta E'$) and angle ($\Delta\theta$). The momentum range covered was $-2.0\% < \Delta E'/E' < 1.0\%$ in 0.1% bins and the $\Delta\theta$ range was -4 mrad $< \Delta\theta < 3$ mrad in 0.5 mrad bins. The counts in each bin were normalized to charge, chamber efficiency, dead time, and the solid angle for that bin. The He inelastic cross section in each bin was calculated by subtracting the end cap and the elastic scattering data from the full target data. At a fixed value of $\Delta E'$, the

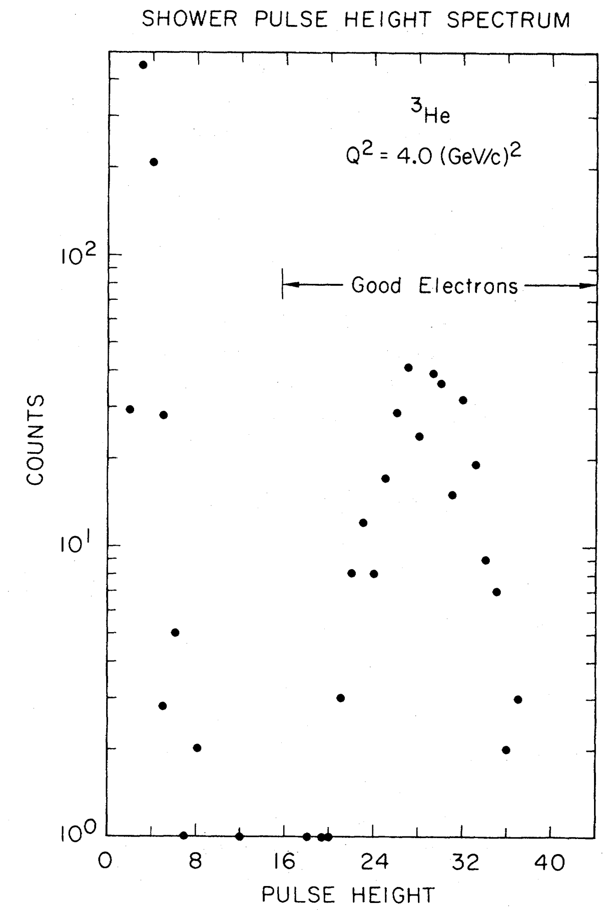

FIG. 3. Shower counter pulse height spectrum for $Q^2=4.0$ data. A showering electron gives a large pulse height which is clearly separated from the small pulse heights due to minimally ionizing heavy particles.

cross section falls approximately a factor of 3 when $\Delta\theta$ varies from -4 mrad to $+3$ mrad. The Mott cross section accounts for a variation of only 20%. Hence, a factor of approximately 2.5 is due to the inelastic structure function. Over the 7 mrad θ acceptance of the spectrometer, this variation is approximately equal to $\theta^{-18} \sim (Q^2)^{-9}$ for fixed E and E'. With such a large cross section variation across the θ acceptance, it is necessary to be very specific about the value of θ at which the results are extracted. However, to use only the data in a very small $\Delta\theta$ slice would reduce the statistical accuracy considerably. The method we chose was to fit the cross sections to a polynomial function of θ at each of the E' values. This is similar to the second method for the calibration analysis. Thus the value of the cross section at $\theta = 8°$ is determined from a fit for each value of E'. The statistical error comes from the fit. Very near threshold and for $Q^2 \geq 3$ (GeV/c)^2 there is insufficient statistical accuracy to use the fitting procedure. The data in these regions were summed over θ and then corrected for the θ dependence found in the regions of high statistical accuracy. An additional systematic error of 7% was added to these data points.

Radiative corrections were made using an unfolding method suggested by Crannell[15] with the radiative correction formulas given by Tsai.[13] This correction increased the cross section by a factor of approximately 1.6 for the low pressure target and 2.1 for the high pressure target. We assign a systematic error of 2% to cover uncertainties in radiator thickness. An additional 3% error is estimated for uncertainties in the theoretical models.[16]

C. Background

The background from the He elastic scattering was small everywhere. It was largest at low Q^2 and negligible above $Q^2=2$ (GeV/c)^2. The double arm acceptance for elastic scattering events was considerably different than the single-arm, 20 GeV spectrometer acceptance. Therefore the double arm elastic events could not be directly subtracted from the 20 GeV single arm data. We generated single arm elastic distributions using a model which included effects of finite resolution and the radiative tail. These distributions were then normalized to the elastic cross sections measured in the double arm portion of the experiment and subtracted from the inclusive data.

The background from the Al end caps was determined at each Q^2 from data taken with the thick-window, empty-target cell. Even though the integrated density of the end caps of the full target was less than 8% of the integrated density of the He inside, the end caps contributed between 50% (near threshold) and 15% (far from threshold) of the full target data. This relatively large end-cap background is present because the kinematics for threshold inelastic e —He scattering corresponds to E' several hundred MeV from inelastic threshold in Al.

One example of the contributions from the full target, Al end caps, and elastic scattering for ^{3}He at $Q^2=1.4$ (GeV/c)^2 is shown in Fig. 4. Ideally in the

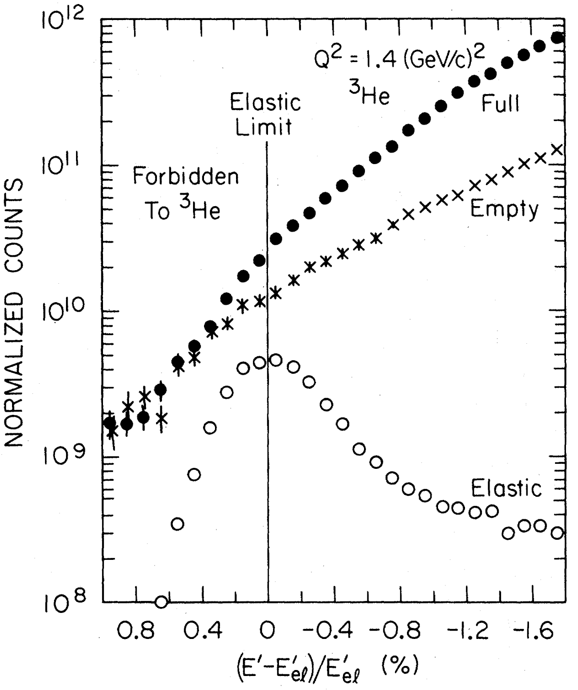

FIG. 4. Total counts and empty-target and elastic scattering backgrounds as a function of scattered electron momentum ($\Delta E'/E'$) for the $Q^2=1.4$ ^{3}He data. The elastic ^{3}He counts are derived from the double arm measurement as described in the text.

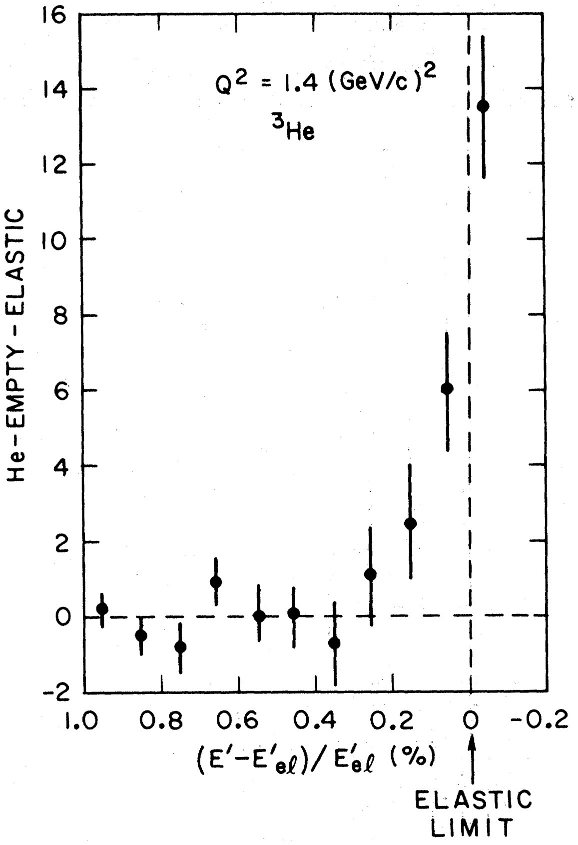

FIG. 5. The inelastic cross section ($\sigma_{\rm tot}-\sigma_{\rm el}-\sigma_{\rm empty}$) as a function of scattered electron momentum ($\Delta' E/E'$) in the unphysical region beyond the elastic limit. The finite resolution of the system manifests itself as a positive cross section for $0 > \Delta E'/E' > 0.1\%$.

unphysical region of $\Delta E'/E' > 0$, the cross section should be zero. Experimentally the finite resolution of beam energy ($\Delta E/E \sim \pm 0.2\%$) and spectrometer ($\Delta E'/E' \sim \pm 0.05\%$) cause the smearing of nonzero cross sections into the unphysical region. This is illustrated in Fig. 5 for the typical case of ^{3}He at $Q^2 = 1.4$ (GeV/c)^2 where the cross section in the unphysical region is plotted versus momentum $\Delta E'/E'$. As expected, the cross section is zero except at $\Delta E'/E' = 0.1\%$, where resolution effects will contribute. Thus the end cap background is subtracted properly.

The 1.8% ^{4}He contamination of the ^{3}He gas also contributed a background to the ^{3}He measurement. Using the ^{4}He cross sections for $Q^2 \leq 1.8$ (GeV/c)^2, this background was found to be between 7% (near threshold) and 4% (far from threshold). The enhancement of the 1.8% contamination is a threshold effect similar to that for the aluminum. This background has been subtracted from the ^{3}He cross sections.

D. Resolution and energy calibration

The experimental resolution is dominated by the energy spread of the incoming electron beam. The incident momentum defining slits were set to be between 0.2% and 0.6% $\Delta E/E$ full width depending on Q^2. The wide slit settings were used for maximum beam intensity at large Q^2 for the elastic measurement going on concurrently.

The He inelastic structure function is a rapidly changing function of $\nu = E - E'$ and slowly varying function of Q^2. At fixed θ it increases by approximately 25% for each 0.1% increase in ν. On the other hand, an uncertainty of 0.1% in E or E' causes an uncertainty of 0.1% in Q^2 which implies only a 1% uncertainty in the structure function. Because of this ν dependence, it is very important to calibrate the beam-spectrometer momentum. This is done by looking at the elastic e-He cross section measured simultaneously and at the elastic e-p data taken with the same beams.

The location of the center of the measured He elastic peaks relative to the expected value of $W^2 = M_{^3\mathrm{He}}{}^2$ depends on both the incident and scattered electron energies. Typically, the elastic peak is located as expected with an uncertainty in $W^2 \sim \pm 0.01$ GeV^2 ($\pm 0.02\%$ $\Delta E/E$) for ^{3}He and ± 0.02 GeV^2 ($\pm 0.03\%$ $\Delta E/E$) for ^{4}He. For $Q^2 \leq 1.8$ (GeV/c)^2 there are enough elastically scat-

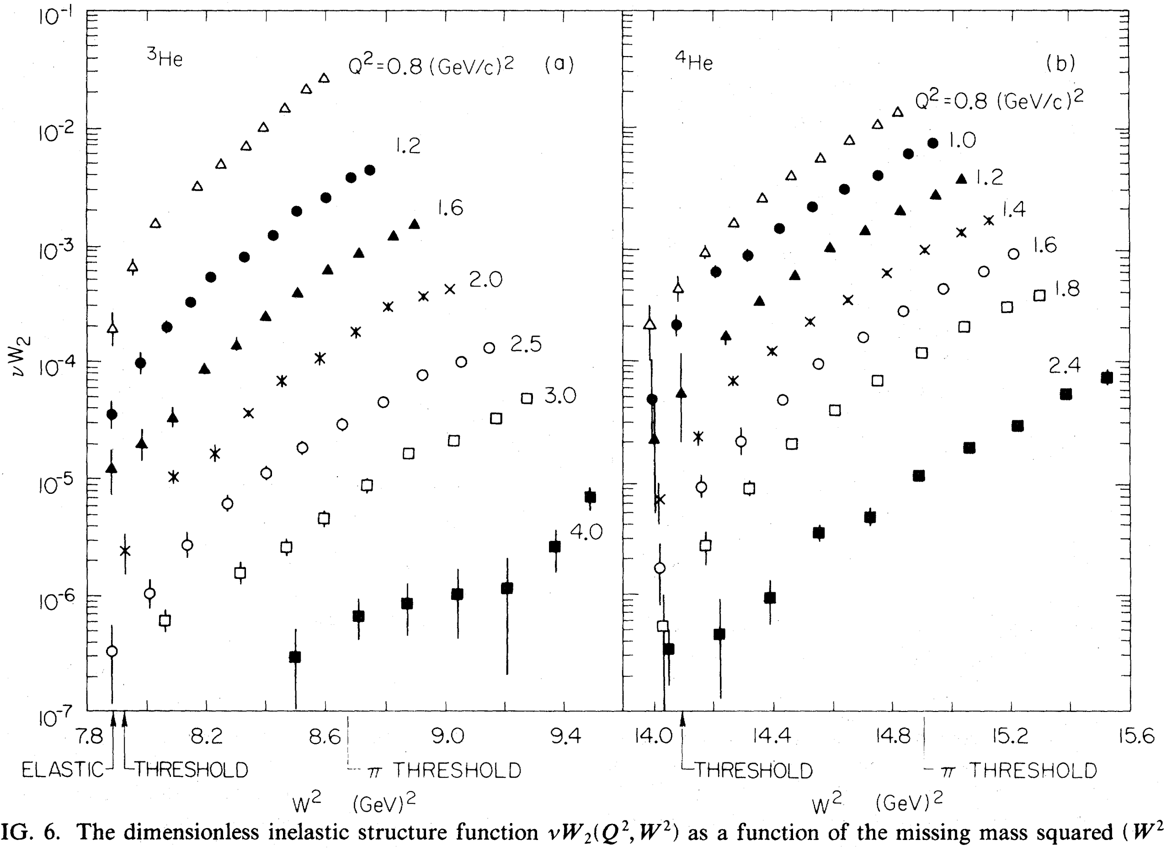

FIG. 6. The dimensionless inelastic structure function $\nu W_2(Q^2, W^2)$ as a function of the missing mass squared (W^2) for several values of the momentum transfer squared (Q^2), (a) ^{3}He and (b) ^{4}He.

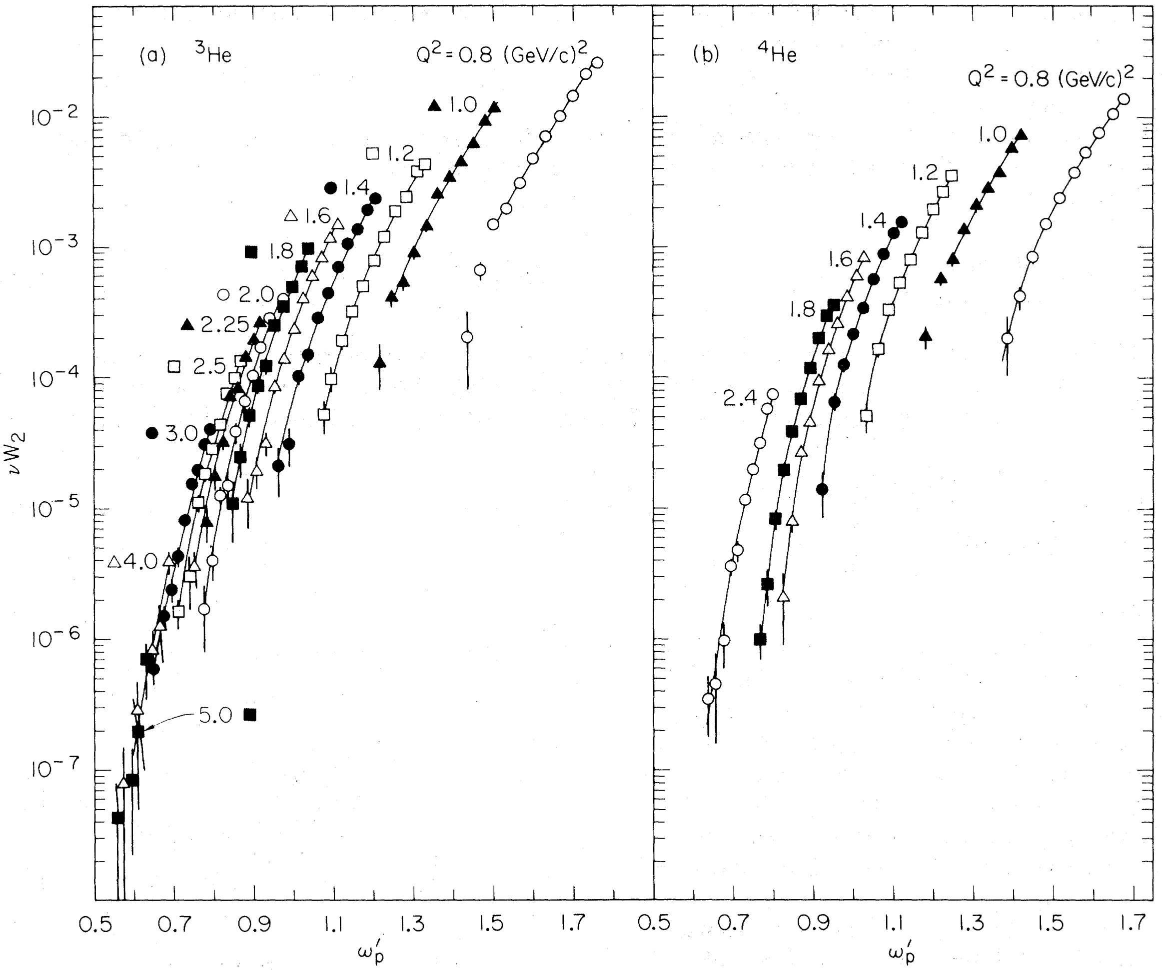

FIG. 7. The inelastic structure function νW_2 as a function of the scaling variable $\omega_p' = 1+(M_p{}^2+2M_p\nu - Q^2)/Q^2$ for several different values of Q^2. The curves at fixed Q^2 are to guide the eye and they seem to approach a common limit, (a) ^{3}He and (b) ^{4}He.

tered electrons from the He target to determine the centroids of the elastic peaks and the momentum scale is calibrated to within approximately $\pm 0.02\%$. For Q^2 up to 2.5 (GeV/c)^2 the proton elastic data was also used for calibration. The elastic proton peaks were found to be offset by $W^2 \sim 0.006 \pm 0.010$ GeV^2 ($0.03 \pm 0.06\%$ $\Delta E/E$) from $W^2 = M_p^2$. Thus for the inelastic He data for $2.0 \leq Q^2 \leq 2.5$ (GeV/c)^2 we estimate a momentum uncertainty of approximately $\pm 0.04\%$ $\Delta E/E$. Above $Q^2 = 2.5$ GeV^2 no proton data were taken and we estimate an uncertainty of approximately $\pm 0.05\%$ $\Delta E/E$.

The width of the elastic peak primarily reflects the beam energy spread. Typically, the elastic peak width for both He and proton elastic scattering data corresponds to an energy spread of FWHM $= 0.2\%$ at low Q^2 and FWHM $= 0.4\%$ at high Q^2. The convolution of the finite resolution with the rapidly changing inelastic cross section increases the cross section by less than 15% at high Q^2 at threshold and by negligible amounts at low Q^2 and far from threshold. This systematic shift is well within the statistical uncertainty.

The above discussion dealt with the momentum reconstruction and solid angle at the center of the spectrometer acceptance at the elastic peaks. Another source of uncertainty is the accuracy of the momentum reconstruction and solid angle away from the center. To check this, He data were taken with the spectrometer offset by 1% in momentum. The cross sections taken with the two different settings agreed within errors. This, combined with the proton calibration of the solid angle in the central momentum region of the spectrometer, indicates a possible systematic uncertainty in the solid angle of approximately 4%. Alternatively, the agreement of the two settings implies that the momentum scale is accurate away from the central region to approximately ± 0.02%. Thus the combined absolute momentum scale is accurate with an uncertainty of between ±0.02% and ±0.05% depending on Q^2. This corresponds to an uncertainty in the cross section of between 4% and 12%. These systematic uncertainties are listed in Table II along with the other systematic errors.

IV. RESULTS AND DISCUSSION

A. Formalism

The cross section for inelastic electron scattering can be written as:

$$\sigma(\Omega,E')=\frac{\alpha^2\cos^2(\theta/2)}{4E^2\sin^4(\theta/2)}\{W_2(\nu,Q^2)+2\tan^2(\theta/2)W_1(\nu,Q^2)\}\ , \tag{4.1}$$

where W_1 and W_2 are the inelastic structure functions, E is the primary beam energy, E' is the scattered electron energy, $\nu=E-E'$, θ is the scattered electron angle, $Q^2=4EE'\sin^2(\theta/2)$ is the four-momentum transfer squared, and $\alpha=\frac{1}{137}$ is the fine structure constant. The elastic scattering cross section can be written as:

$$\sigma(\Omega)=\frac{Z^2\alpha^2\cos^2(\theta/2)}{4E^2\sin^4(\theta/2)\left[1+\frac{2E}{M}\sin^2(\theta/2)\right]}\{A(Q^2)+B(Q^2)\tan^2(\theta/2)\}\ . \tag{4.2}$$

At our experimental angle of $\theta=8°$, the factor $\tan^2(\theta/2)=0.005$ and we shall assume that the W_1 and B structure functions do not contribute significantly to the cross section. Note that Z^2 has been explicitly factored out of the elastic structure functions in Eq. (4.2) and not out of the inelastic structure functions in Eq. (4.1) to be consistent with the Nuclear Physics and High Energy Physics conventions, respectively.

The structure functions and cross sections will be examined below as functions of several variables:

$$\Delta E'/E'_{\rm el}=(E'-E'_{\rm el})/E'_{\rm el}\ ;$$

fractional deviation of electron momentum from the He elastic peak. (Positive values are kinematically forbidden.)

$$W^2=M^2+2M\nu-Q^2\ ;$$

total mass of the outgoing hadronic system (missing mass). For $e-{}^3$He scattering $W^2>M^2({}^3\text{He})=7.885$ GeV^2 and for $e-{}^4$He scattering $W^2>M^2({}^4\text{He})=13.891$ GeV^2.

$$x=Q^2/2M\nu\ ;$$

deep inelastic scaling variable. M is the mass of the target particle.

$$W_p{}^2=M_p{}^2+2M_p\nu-Q^2\ ;$$

mass of the outgoing hadronic system including only one of the nucleons. The others are assumed to be spectators in the reaction.

$$\omega_p'=1+W_p{}^2/Q^2=M_p/xM+M_p{}^2/Q^2\ ;$$

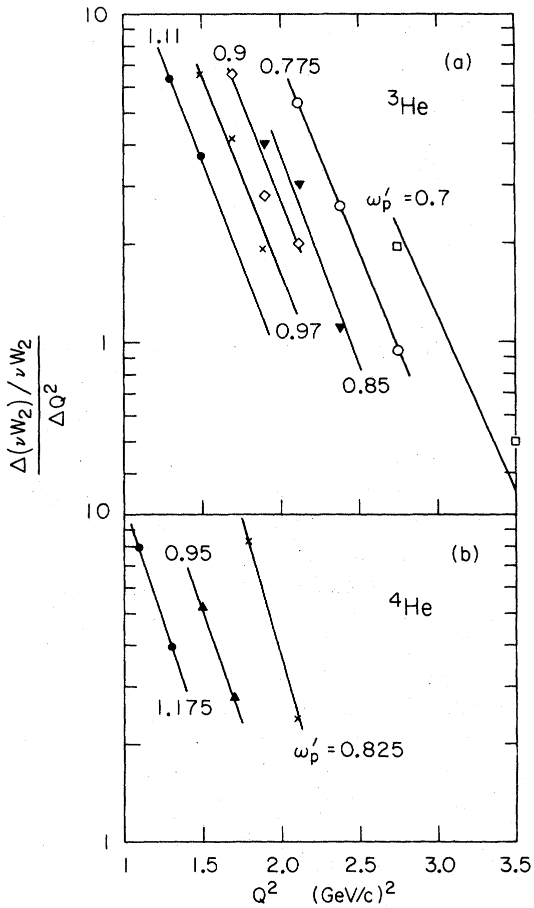

FIG. 8. The relative change $\Delta(\nu W_2)/\nu W_2$ in the structure function νW_2 for a change in Q^2 at fixed values of ω_p' showing the approach to scaling, (a) ^{3}He and (b) ^{4}He.

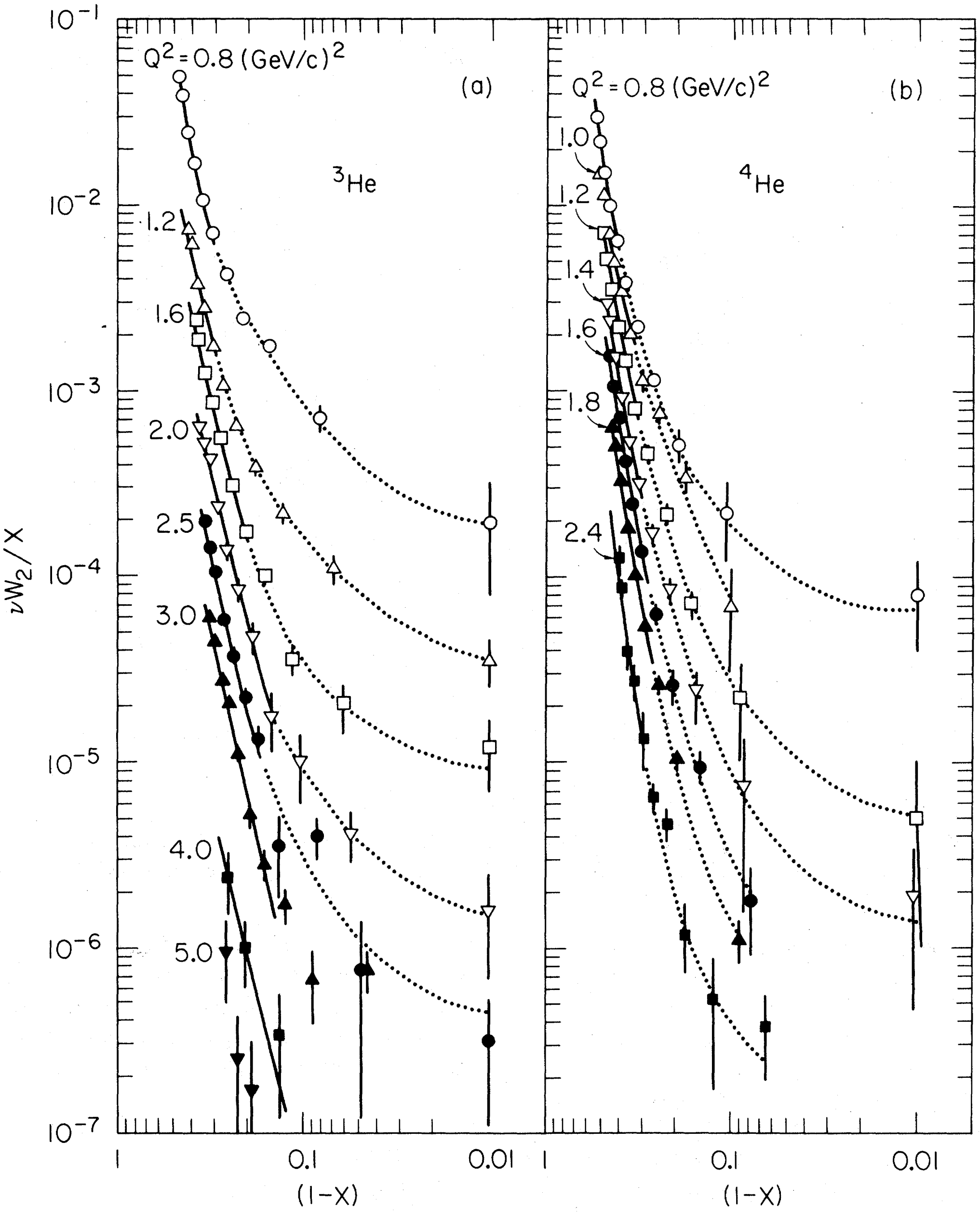

FIG. 9. The threshold behavior of $\nu W_2/x$ as a function of $(1-x)$, the fractional momentum of the spectator system, for several different values of Q^2. The curves are to guide the eye. The solid portions are nearly parallel straight lines corresponding to $\nu W_2 \sim x(1-x)^n$ as discussed in the text, (a) ^{3}He and (b) ^{4}He.

scaling variable for use near threshold. Assume that only one nucleon is active in the reaction. The motivation for using this set of variables comes from deep inelastic electron scattering from nucleons. There the dimensionless form factor $\nu W_2(\nu,Q^2)$ becomes a function of x alone at high Q^2. Closer to the elastic threshold, νW_2 is primarily[17] a function of ω_p'.

B. Data

Our results for νW_2 for ^{3}He and ^{4}He at all Q^2 as a function of W are given in Tables III and IV. A sample of these results for ^{3}He (^{4}He) is shown in Figs. 6(a) and (b) as a function of W^2. The cross sections are smoothly varying functions of W^2. There is no visible effect due to the opening of the π

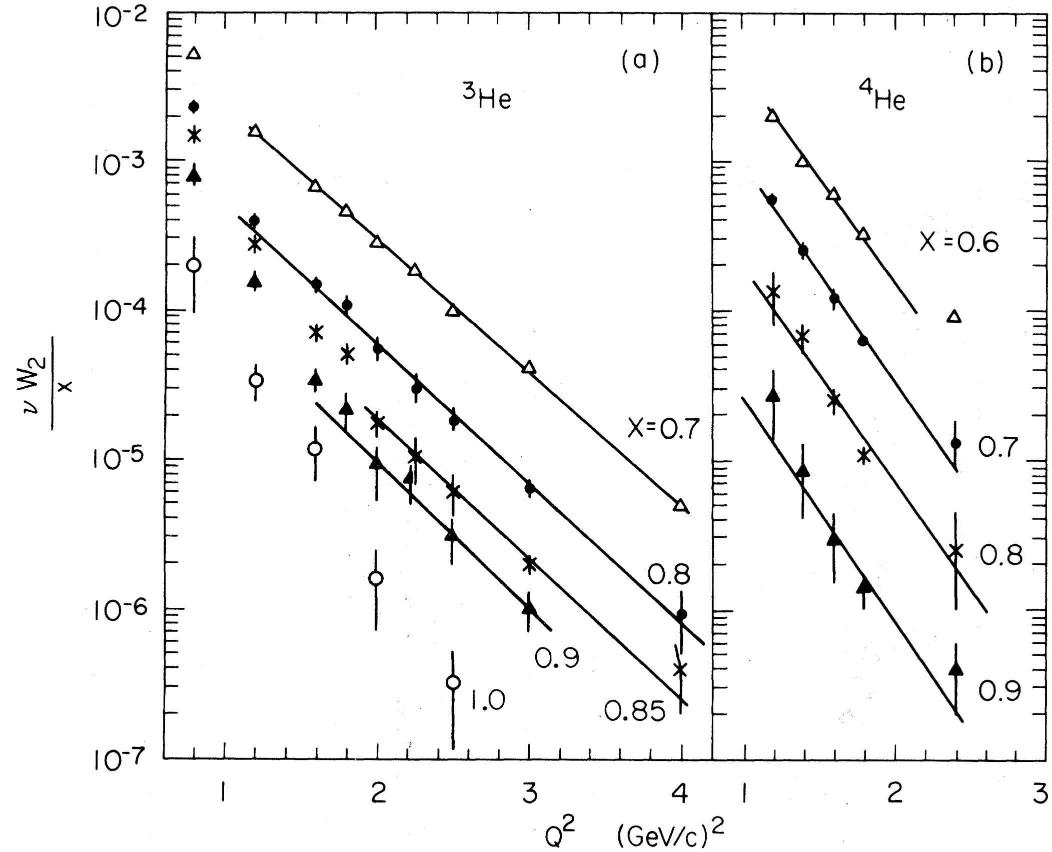

FIG. 10. $\nu W_2/x$ as a function of Q^2 at several values of the scaling variable x. The nearly parallel straight lines indicate a possible exponential behavior at large Q^2 independent of x. The data are also fit by a power law of the form of Eq. (4.8), (a) ^{3}He and (b) ^{4}He.

inelastic channel in either reaction.

Figures 7(a) and (b) show νW_2 as a function of the scaling variable ω_p' for various values of Q^2. As Q^2 increases, the lines at constant Q^2 get closer together and may be approaching an asymptotic scaling curve at very high Q^2. This approach to an asymptotic shape is more obvious for ^{3}He than for ^{4}He because scaling is expected to set in at larger Q^2 in the higher mass number nucleus, and because our data extends to a higher Q^2 for ^{3}He than for ^{4}He. In Figs. 8(a) and (b) the approach to scaling is demonstrated for ^{3}He and ^{4}He. The relative change in νW_2 with Q^2,

$$D=\frac{\Delta(\nu W_2)/\nu W_2}{\Delta Q^2} ,$$

is plotted there as a function of Q^2 for fixed ω_p'. As Q^2 increases, D decreases exponentially, which indicates that $\nu W_2(\omega_p',Q^2)$ is approaching a Q^2 independent limit. This same scaling phenomenon was observed in inelastic $e-d$ scattering.[7]

For the nucleon, the Drell-Yan and West formalism[2] predicts a direct relationship between the power law falloff with Q^2 of the elastic form factor and the rise in the inelastic cross section at threshold. The model is based on scattering from a single off-shell constituent (parton) of fractional momentum x within the nucleon. The structure functions take the form:

$$\nu W_2 \sim x(1-x)^n . \qquad (4.3)$$

$$A(Q^2) \sim (Q^2)^{-(n+1)} , \qquad (4.4)$$

for $x \to 1$ and Q^2, $M\nu \gg M^2$, and where the power n is related to the number of constituents. While our data are not quite in the high Q^2 and large $M\nu$ region appropriate for this model. we are nevertheless motivated to see if the data behave like

$$\nu W_2 \sim x(1-x)^n .$$

This form is a common prediction for the models we want to consider in the next section where n is determined by the number of spectator constituents in the reaction.

In Figs. 9(a) and (b), $\nu W_2/x$ is plotted as a function of $1-x$ on a log-log scale. With increasing Q^2,

TABLE III. The ^{3}He structure function νW_2 at 8° vs the missing mass W in GeV at different incident electron energies. The Q^2 values are for elastic scattering, $W=2.808$ GeV. The numbers in parenthesis are the statistical followed by the systematic errors.

$E=6.483$ GeV [$Q^2=0.8$ (GeV/c)^2]	
W (GeV)	$10^5\nu W_2$
2.808	$16\pm(10,15)$
2.821	$57\pm(10,5)$
2.834	$125\pm(10,10)$
2.847	$165\pm(15,15)$
2.859	$268\pm(20,25)$
2.872	$421\pm(20,40)$
2.887	$620\pm(30,55)$
2.897	$920\pm(35,80)$
2.910	$1300\pm(40,110)$
2.922	$1945\pm(50,170)$
2.932	$2425\pm(90,210)$

$E=8.607$ GeV [$Q^2=1.4$ (GeV/c)^2]	
W GeV	$10^5\nu W_2$
2.808	$2.0\pm(0.8,0.3)$
2.825	$2.9\pm(1.0,0.4)$
2.842	$9.5\pm(1,1)$
2.859	$13.9\pm(1.5,1.5)$
2.876	$27.3\pm(1.9,3)$
2.893	$42.6\pm(2.4,5)$
2.909	$67.5\pm(3.1,6)$
2.926	$102\ \pm(4,10)$
2.942	$131\ \pm(5,12)$
2.959	$187\ \pm(6,15)$
2.971	$229\ \pm(9,20)$

$E=7.257$ GeV [$Q^2=1.0$ (GeV/c)^2]	
W (GeV)	$10^5\nu W_2$
2.808	$10\pm(5,1)$
2.822	$31\pm(7,3)$
2.837	$42\pm(7,5)$
2.851	$74\pm(9,8)$
2.865	$119\pm(11,12)$
2.880	$220\pm(14,20)$
2.894	$295\pm(18,30)$
2.908	$390\pm(20,40)$
2.922	$539\pm(25,50)$
2.936	$802\pm(30,80)$
2.946	$1040\pm(60,100)$

$E=9.210$ GeV [$Q^2=1.6$ (GeV/c)^2]	
W (GeV)	$10^5\nu W_2$
2.808	$1.1\pm(0.5,0.2)$
2.826	$1.8\pm(0.5,0.3)$
2.845	$3.1\pm(0.6,0.5)$
2.863	$8.1\pm(0.8,1.2)$
2.881	$13.5\pm(1,2)$
2.899	$22.8\pm(1.4,2.6)$
2.917	$39.0\pm(1.7,3.7)$
2.934	$57.9\pm(2.2,5.5)$
2.952	$80.4\pm(2.7,7.2)$
2.969	$115\ \pm(3,10)$
2.982	$145\ \pm(6,12)$

$E=7.959$ GeV [$Q^2=1.2$ (GeV/c)^2]	
W (GeV)	$10^5\nu W_2$
2.808	$3.6\pm(1.1,0.5)$
2.824	$10.1\pm(2.3,1.3)$
2.840	$20\ \pm(3,3)$
2.855	$33\ \pm(3,4)$
2.867	$52\ \pm(4,7)$
2.887	$84\ \pm(5,10)$
2.902	$127\ \pm(7,15)$
2.917	$197\ \pm(8,24)$
2.933	$258\ \pm(10,30)$
2.948	$402\ \pm(12,50)$
2.959	$463\ \pm(20,55)$

$E=9.778$ GeV [$Q^2=1.8$ (GeV/c)^2]	
W (GeV)	$10^5\nu W_2$
2.828	$1.0\pm(0.6,0.2)$
2.847	$2.3\pm(0.7,0.3)$
2.866	$4.8\pm(0.8,0.7)$
2.885	$8.3\pm(1.0,1.1)$
2.904	$11.8\pm(1.4,1.5)$
2.923	$23.8\pm(1.6,3)$
2.942	$33.8\pm(2.1,3)$
2.960	$47.7\pm(2.5,4)$
2.979	$68.9\pm(3.1,6)$
2.993	$95.5\pm(4.8,8)$

the data approach a straight line over an ever larger region of x. The solid curves in Fig. 9 show this power law dependence of Eq. (4.3). $n=4.1\pm0.5$ for ^{3}He for $x\lesssim0.85$ and $n=6.0\pm0.5$ for ^{4}He for $x\lesssim0.75$. The dashed lines guide the eye through the other data points at the same Q^2. For ^{3}He at the highest values of Q^2, the entire data set follows the power law, while at $Q^2=1.6$ half the points fall on a straight line covering an order of magnitude change in $\nu W_2/x$. For ^{4}He the linear region is more limited. Some models (see the next section) have a sum of terms with different powers of $(1-x)$ which may explain the deviations from straight lines in Fig. 9.

Figures 10(a) and (b) show $\nu W_2/x$ as a function of Q^2 for several different values of x. For each isotope the data falls exponentially as a function of Q^2 with an exponent which is independent of x. A

TABLE III. (*Continued.*)

$E=10.316$ GeV $[Q^2=2.0\ (\text{GeV})/c)^2]$

W (GeV)	$10^5 \nu W_2$
2.808	$0.15\pm(0.09,0.03)$[a]
2.828	$0.38\pm(0.12,0.07)$[a]
2.849	$0.88\pm(0.39,0.15)$
2.869	$1.4\ \pm(0.5,0.3)$
2.889	$3.7\ \pm(0.7,0.6)$
2.909	$6.4\ \pm(0.9,0.9)$
2.929	$9.9\ \pm(1.2,1.3)$
2.949	$16.5\ \pm(1.5,2.2)$
2.969	$28.1\ \pm(1.9,3.5)$
2.988	$33.2\ \pm(2.3,4.0)$
3.002	$39.3\ \pm(3.9,4.6)$

$E=10.954$ GeV $[Q^2=2.25\ (\text{GeV}/c)^2]$

W (GeV)	$10^5 \nu W_2$
2.808	$0.04\pm(0.05,0.007)$[a]
2.830	$0.17\pm(0.16,0.03)$
2.851	$0.67\pm(0.22,0.11)$
2.873	$0.75\pm(0.27,0.12)$
2.894	$1.7\ \pm(0.3,0.3)$
2.915	$3.1\ \pm(0.4,0.4)$
2.936	$7.0\ \pm(0.6,0.9)$
2.957	$8.2\ \pm(0.7,1.1)$
2.978	$14.0\ \pm(0.9,1.7)$
2.999	$19.3\ \pm(1.2,2.3)$
3.014	$25.5\ \pm(2,3)$

$E=11.558$ GeV $[Q^2=2.5\ (\text{GeV}/c)^2]$

W (GeV)	$10^5 \nu W_2$
2.808	$0.030\pm(0.021,0.005)$[a]
2.831	$0.094\pm(0.03,0.016)$[a]
2.854	$0.34\ \pm(0.09,0.06)$
2.876	$0.29\ \pm(0.13,0.05)$
2.899	$1.1\ \pm(0.2,0.2)$
2.921	$1.7\ \pm(0.2,0.2)$
2.943	$2.8\ \pm(0.3,0.4)$
2.965	$4.2\ \pm(0.3,0.5)$
2.987	$7.4\ \pm(0.4,0.9)$
3.009	$9.6\ \pm(0.6,1.1)$
3.025	$13.0\ \pm(0.9,1.5)$

$E=12.685$ GeV $[Q^2=3.0\ (\text{GeV}/c)^2]$

W (GeV)	$10^5 \nu W_2$
2.808	$0.018\pm(0.017,0.003)$[a]
2.833	$0.069\pm(0.017,0.013)$[a]
2.858	$0.059\pm(0.027.0.011)$[a]
2.883	$0.14\ \pm(0.03,0.03)$[a]
2.908	$0.23\ \pm(0.05,0.04)$[a]
2.932	$0.42\ \pm(0.07,0.06)$[a]
2.956	$0.86\ \pm(0.19,0.13)$
2.980	$1.4\ \pm(0.2,0.2)$
3.004	$1.8\ \pm(0.3,0.3)$
3.028	$3.6\ \pm(0.4,0.5)$
3.045	$4.7\ \pm(0.6,0.7)$

$E=14.696$ GeV $[Q^2=4.0\ (\text{GeV}/c)^2]$

W (GeV)	$10^5 \nu W_2$
2.844	$0.008\pm(0.007,0.002)$[a]
2.916	$0.028\pm(0.019,0.004)$[a]
2.951	$0.062\pm(0.025,0.01)$[a]
2.979	$0.081\pm(0.040,0.01)$[a]
3.007	$0.10\ \pm(0.06,0.01)$[a]
3.034	$0.11\ \pm(0.09,0.02)$[a]
3.061	$0.24\ \pm(0.10,0.04)$[a]
3.081	$0.66\ \pm(0.14,0.1)$[a]

$E=16.479$ GeV $[Q^2=5.0\ (\text{GeV}/c)^2]$

W (GeV)	$10^5 \nu W_2$
3.007	$0.006\pm(0.008,0.008)$[a]
3.075	$0.024\pm(0.015,0.004)$[a]
3.113	$0.07\ \pm(0.05,0.01)$[a]

[a] Analyzed by summing over the spectrometer angular acceptance as discussed in Sec. III B of text.

power law dependence of Q^2 also fits the data quite well (see Sec. IV C). In either case νW_2 can be factored into a function of x times a function of Q^2.

C. Theoretical models

In this section the data is compared with some models which incorporated dimensional scaling[18] and factorization of the scattering amplitude. To date the models suggested for high energy inclusive electron nucleus interactions are mainly phenomenological in nature. They are generalizations of the quark-proton model of hadrons which have been applied to nuclei. They are constructed to agree with the asymptotic limits at very high energy and they are presented with the idea of giving an approximate picture of a wide variety of data.

TABLE IV. The ^{4}He structure function νW_2 at 8° vs the missing mass W in GeV at different incident electron energies. The Q^2 values are for elastic scattering, $W=3.727$. The numbers in parenthesis are the statistical followed by the systematic errors.

$E=6.465$ GeV [$Q^2=0.8$ (GeV/c)^2]		$E=7.235$ GeV [$Q^2=1.0$(GeV/c)^2]		$E=7.933$ GeV [$Q^2=1.2$ (GeV/c)^2]	
W GeV	$10^5\nu W_2$	W (GeV)	$10^5\nu W_2$	W (GeV)	$10^5\nu W_2$
3.739	28±(10,3)	3.740	10±(3,1)[a]	3.726	0.5±(0.5,0.04)[a]
3.752	58±(10,5)	3.755	23±(5,2)	3.742	2.1±(1.6,0.2)
3.765	127±(13,12)	3.769	54±(7,5)	3.758	6.6±(1.7,0.6)
3.777	210±(17,20)	3.783	78±(9,7)	3.773	17 ±(2,1)
3.790	352±(23,35)	3.798	134±(12,12)	3.789	33 ±(3,3)
3.803	505±(30,50)	3.812	210±(16,20)	3.804	53 ±(4,4)
3.815	778±(35,80)	3.826	290±(20,25)	3.820	90 ±(5,7)
3.828	1110±(50,110)	3.840	393±(23,30)	3.835	129 ±(6,10)
3.841	1590±(60,150)	3.854	606±(30,50)	3.851	193 ±(8,15)
3.850	2110±(100,200)	3.864	760±(52,60	3.866	267 ±(10,21)
				3.878	355 ±(17,28)

$E=8.576$ GeV [$Q^2=1.4$ (GeV/c)^2]		$E=9.175$ GeV [$Q^2=1.6$ (GeV/c)^2]		$E=9.738$ GeV [$Q^2=1.8$ (GeV/c)^2]		$E=11.267$ GeV [$Q^2=2.4$ (GeV/c)^2]	
W GeV	$10^5\nu W_2$	W (GeV)	$10^5\nu W_2$	W (GeV)	$10^5\nu W_2$	W (GeV)	$10^5\nu W_2$
3.743	0.68±(0.54,0.06)	3.744	0.25±(0.11,0.02)[a]	3.750	0.10±(0.03,0.02)[a]	3.748	0.034±(0.017,0.006)[a]
3.760	2.0 ±(0.7,0.2)	3.763	0.81±(0.15,0.11)[a]	3.784	0.83±(0.12,0.12)[a]	3.771	0.045±(0.032,0.008)[a]
3.777	6.6 ±(1.1,0.6)	3.781	2.1 ±(0.5,0.3)	3.803	2.0 ±(0.2,0.3)[a]	3.793	0.094±(0.04,0.015)[a]
3.794	12.4 ±(1.4,1.0)	3.799	4.7 ±(0.8,0.6)	3.822	4.0 ±(0.4,0.5)[a]	3.815	0.34 ±(0.05,0.05)[a]
3.811	21.5 ±(1.9,1.7)	3.817	96. ±(1.1,1.0)	3.841	7.0 ±(0.6,0.9)[a]	3.837	0.47 ±(0.09,0.07)[a]
3.828	33.8 ±(2.6,2.7)	3.835	16.3 ±(1.4,1.5)	3.860	12.0 ±(1,1.5)[a]	3.859	0.9 ±(0.3,0.1)[a]
3.844	56.3 ±(3.2,4.5)	3.852	26.3 ±(1.9,2)	3.879	20.5 ±(2,2.5)[a]	3.881	1.8 ±(0.4,0.2)[a]
3.861	87.3 ±(4.1,7)	3.870	42.0 ±(2.6,4)	3.897	30.5 ±(3,3.5)[a]	3.902	2.5 ±(0.5,0.3)[a]
3.877	128 ±(5,10)	3.888	59.9 ±(3.2,5)	3.911	37 ±(3,4)[a]	3.924	5.3 ±(0.6,0.6)[a]
3.890	153 ±(9,12)	3.901	83.7 ±(5.6,7)			3.940	7.3 ±(1.1,0.8)[a]

[a] Analyzed by summing over the spectrometer angular acceptance as discussed in Sec. III B of text.

While it is premature to use these models to extract detailed information from our data, they can motivate our understanding of the basic questions; namely, what constituents (nucleons, clusters of nucleons, quarks) interact with the virtual photon; what are the interactions between the constituents in the initial and final states; what are the spacial and momentum distributions of the constituents in nuclei?

It was proposed in a study of the asymptotic form factors and the connection of nuclear and nucleon dynamics[3] that the inelastic scattering near threshold takes place via the elastic scattering from individual nucleons within the nucleus. The prediction is

$$\sigma(Q^2,x)(eA\to e'X)=\sum_{i=1}^{A}\sigma(Q^2)(eN\to e'N)\times G_{N_i/A}(x)\ , \qquad (4.5)$$

where $G_{N_i/A}(x)$ is the probability for the ith nucleon to have fractional momentum x in the infinite momentum frame of the nucleus A. This can be rewritten in terms of the form factors

$$\nu W_2=\sum_{i=1}^{A}A_n(Q^2)xG_{N_i/A}(x)\ , \qquad (4.6)$$

where $A_n(Q^2)$ is the elastic nucleon structure function. If one term in Eq. (4.6) dominates, the inelastic cross section would then factor into a function of x times a function of Q^2 as noted in Sec. IV B. The quark-spectator counting rules[19] were generalized in Ref. 3 for nucleons in nuclei to give

$$G_{N_i/A}(x)\sim(1-x)^{6(A-1)-1}\ ,$$

which is valid for $x\to1$, where A is the atomic weight of the nucleus. At fixed W (including the elastic limit) for $x\to1$ and large Q^2 where $(1-x)\to(W^2-M^2)/Q^2$, each term in the sum falls with the same power of Q^2 as given by the dimensional scaling quark model (DSQM).

Others[4,20] have extended some of these ideas to include scattering from clusters of nucleons within nuclei in analogy with scattering from quarks and diquarks within the nucleon. For large x Schmidt and Blankenbecler[4] derive the form

$$G(x)\sim(1-x)^{2T(A-a)_{\text{eff}}-1} \qquad (4.7)$$

for the interaction of the virtual photon with a cluster of a nucleons in the nucleus of atomic number A, leaving the remaining $(A-a)$ nucleons as spectators. If some or all of the spectator nucleons are bound in clusters then $(A-a)_{\text{eff}}$ is the effective number of spectators in the final state. The factor T is a theory dependent parameter which has been experimentally determined to be approximately three (corresponding to the exchange of vector mesons between nucleons with monopole form factors) from a variety of nucleus-nucleus scattering experiments. They note that $T=3$ is the same result as from quark constituent counting. The nucleon elastic structure function $A_n(Q^2)$ in Eq. (4.6) is replaced by the elastic form factor $A_a(Q^2)$ of the struck nucleon or cluster a.

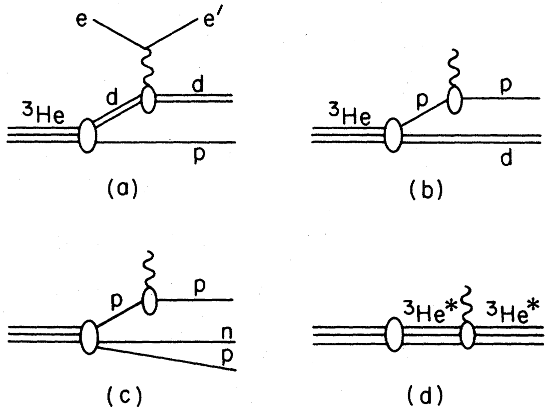

FIG. 11. Possible mechanisms for electron scattering from the constituents of the ^{3}He nucleus.

Examples of some of these processes are shown for ^{3}He and ^{4}He in Figs. 11 and 12. The values of n determined from the $(1-x)^n$ dependence of $\nu W_2/x$

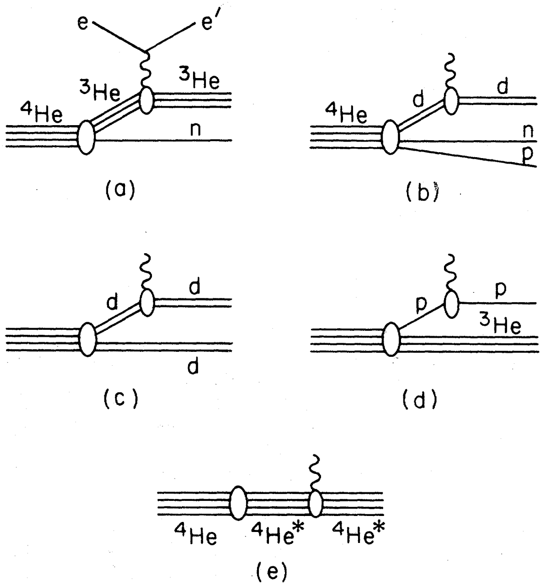

FIG. 12. Possible mechanisms for electron scattering from the constituents of the ^{4}He nucleus.

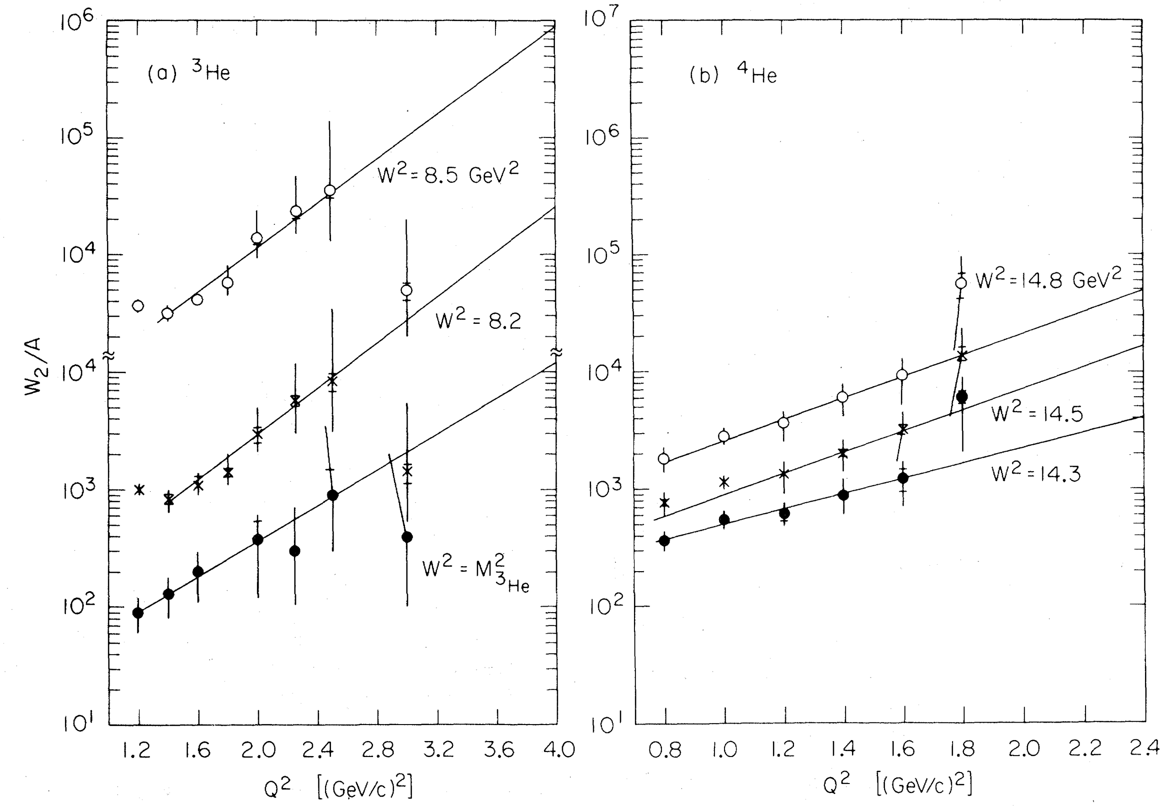

FIG. 13. The elastic-inelastic connection. $W_2(Q^2,W^2)/A(Q^2)$ in units of GeV^{-1} as a function of Q^2 for several fixed values of W^2, where W_2 and A are the inelastic and elastic structure functions, respectively. The lines indicate the extrapolation to high Q^2 used in the text, (a) ^{3}He and (b) ^{4}He.

described in Sec. IV B gives $(A-a)_{\text{eff}}(^3\text{He}) = 0.9 \pm 0.1$ and $(A-a)_{\text{eff}}(^3\text{He}) = 1.2 \pm 0.1$. This implies the dominance of diagrams with twofold breakup such as those shown in Figs. 11(a), 11(b), 12(a), 12(c), and 12(d). The Q^2 dependence comes primarily from the cluster elastic form factors $A_a(Q^2)$ for this Q^2 and x range. Using the DSQM with mass corrections[3] the elastic form factors are given by

$$
\begin{aligned}
&[A_p(Q^2)]^{1/2} \sim F_p = (1+Q^2/0.71)^{-2} , \\
&[A_d(Q^2)]^{1/2} \sim F_d = (1+Q^2/1.41)^{-5} , \qquad (4.8) \\
&[A_{^3\text{He}}(Q^2)]^{1/2} \sim F_{^3\text{He}} = (1+Q_2/2.1)^{-8} ,
\end{aligned}
$$

We note that the photon-hadron vertices in Figs. 11 and 12 are for hadronic matter way off the mass shell, whereas the DSQM form factors are on mass shell. The best fit to the ^{3}He data displayed in Fig. 10(a) for $x \leq 0.9$ using these forms is $(1+Q^2/1.41)^{-n}$ with $n = 4.5 \pm 0.5$. This indicates dominance of the diagram in Fig. 11(a), the $d-p$ breakup. The d can be any dinucleon configuration, not necessarily the deuteron. For ^{4}He the form $(1+Q^2/1.41)^{-n}$ with $n = 5.5 \pm 0.5$ gives the best fit of this type to the data in Fig. 10(b). This points to the dominance of the diagram in Fig. 12(c), the $d-d$ breakup, where again d is any dinucleon. Note that this latter diagram is not consistent with dimensional scaling if extrapolated to large Q^2 and $x \to 1$ because it falls asymptotically as $(Q^2)^{-15}$ instead of the predicted $(Q^2)^{-2}$. This inconsistency may be due to our leaving out a slowly varying vertex function of Q^2 that depends on the spectator configuration.

Very close to $x = 1$, the diagrams in Figs. 11(d) and 12(e), corresponding to trinucleon or quadnucleon correlations, may dominate because of their $(1-x)^{-1}$ behavior. This may be indicated in the data where the $1-x$ dependence flattens out near $x = 1$ as shown in Figs. 9(a) and (b).

D. Elastic-inelastic connection

The inelastic data near threshold can be compared with the elastic cross section using the elastic-inelastic connection[3]:

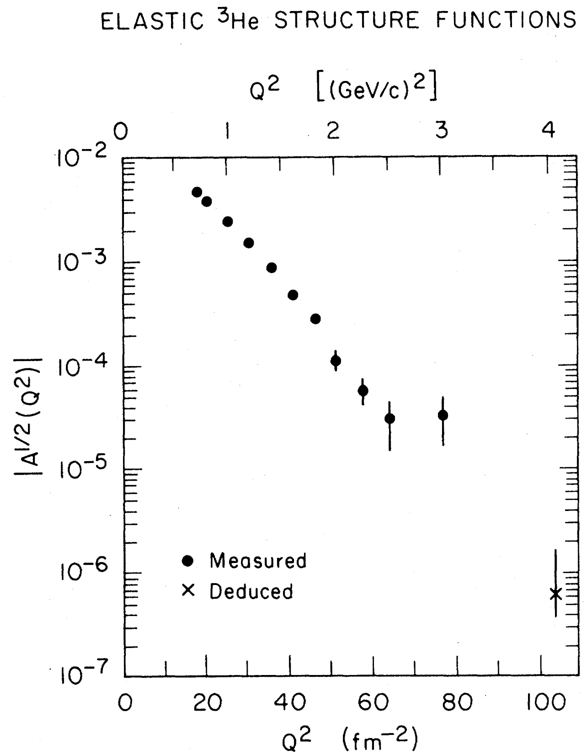

FIG. 14. The elastic structure function $A(Q^2)$ for ^{3}He as a function of Q^2 showing previously directly measured values (Ref. 1) and the highest Q^2 value derived from the elastic-inelastic connection.

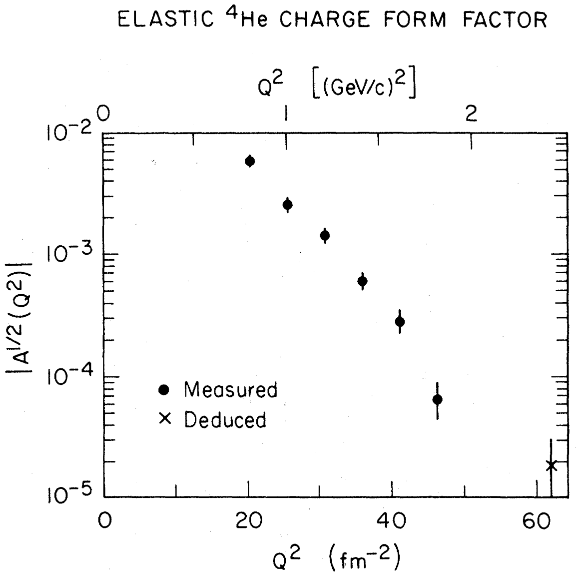

FIG. 15. The elastic structure function $A(Q^2)$ for ^{4}He as a function of Q^2 showing previously directly measured values (Ref. 1) and the highest Q^2 value derived from the elastic-inelastic connection.

$$\sigma(Q^2,W^2)=\sigma(Q^2)\Big|_{\text{elastic}}\rho(W^2)\,, \tag{4.9}$$

where ρ is an unknown function of W^2 only. Near threshold this can be simplified to

$$W_2=2MA(Q^2)\rho(W^2)\,, \tag{4.10}$$

where $A(Q^2)$ is the elastic structure function from Eq. (4.2). Figures 13(a) and (b) show the ratio $W_2/A(Q^2)$ at several values of W^2 for ^{3}He and ^{4}He, respectively. The shorter error bars are those due to the inelastic cross section while the extended error bars include the dominating elastic scattering errors (Ref. 1). Within the large errors the results for ^{3}He are consistent with both a steady rise in the ratio above $Q=1.4$ (GeV/c)^2 or a flat ratio above $Q^2=1.8$ (GeV/c)^2. The interpretation is difficult because the elastic data at $Q^2=3$ (GeV/c)^2 is only one event. For ^{4}He, the data are consistent with a steady rise of $W_2/A(Q^2)$. This is in marked contrast to the $e-d$ data (Ref. 7), where $W_2/A(Q^2)$ approaches a constant for $Q^2\geq 2.5$ (GeV/c)^2. Extrapolating the steady rise of W_2/A in the ^{3}He (^{4}He) data to $Q^2=4.0$ (2.4) (GeV/c)^2 and using the measured values of νW_2 yields $A^{1/2}(^3\text{He})\ \sim 7^{+10}_{-3}\times 10^{-7}$ and $A^{1/2}(^4\text{He})\sim(2\pm 1)\times 10^{-5}$. These values are shown along with the directly measured elastic form factors at lower Q^2 in Figs. 14 and 15. The new points are consistent with the exponentially falling elastic form factors discussed in Ref. 1.

In conclusion, these results are consistent with an approach to scaling in the variable ω_p', although the full application of asymptotic quark models has to await higher Q^2 data. A model based on scattering from clusters of nucleons within the nucleus is also consistent with the data. Future research can be profitably directed toward measurement of the other structure functions $W_1(\nu,Q^2)$ and determination of the configuration of the hadronic fragments in experiments where the electrons are measured in coincidence with recoil particles.

ACKNOWLEDGMENTS

We are pleased to acknowledge many people at SLAC for their assistance in setting up and running this experiment. In particular, we thank W. P. Schütz for initial high pressure target design and C. Hoard, J. Mark, S. St. Lorant, and the SLAC target group for design, construction, and maintenance of the targets. We also thank C. Sinclair, L. Boyer, R. Eisele, S. Dyer, D. Sherden, and the Spectrometer Facilities Group for assistance in setting up the spectrometers. This investigation was supported in part by the National Science Foundation, Grant No. PHY78-09378.

---

*Deceased 1981.

[1] R. G. Arnold *et al.*, Phys. Rev. Lett. 40, 1429 (1978).

[2] S. D. Drell and T. M. Yan, Phys. Rev. Lett. 24, 181 (1970); G. B. West, *ibid.* 24, 1206 (1970).

[3] S. J. Brodsky and B. T. Chertok, Phys. Rev. D 14, 3003 (1976).

[4] I. Schmidt and R. Blankenbecler, Phys. Rev. D 15, 3321 (1977); 16, 1318 (1977); R. Blankenbecler, in *Recent Developments in Particle and Field Theory,* edited by W. Dittrich (Vieweg, Wiesbaden, 1979).

[5] L. L. Frankfurt and M. I. Strikman, Phys. Lett. 69B, 93 (1977).

[6] L. L. Frankfurt and M. I. Strikman, Leningrad Nuclear Physics Institute Report 559, 1980.

[7] W. P. Schütz *et al.*, Phys. Rev. Lett. 38, 259 (1977).

[8] D. Day, Ph.D. thesis, University of Virginia, Charlottesville, 1979.

[9] R. D. McCarthy, National Bureau of Standards Technical Note G31, 1972.

[10] L. Mo, SLAC Report No. SLAC Tn-65-40, 1965; S. Stein *et al.*, Phys. Rev. D 12, 1884 (1975).

[11] SLAC Users Handbook and E. A. Taylor, SLAC Technical Note 71-26, 1977.

[12] M. Mestayer, SLAC Report No. 214, 1978.

[13] Y. S. Tsai, SLAC Report No. SLAC-Pub-848, 1971; L. M. Mo and Y. S. Tsai, Rev. Mod. Phys. 41, 205 (1969).

[14] F. Iachello, A. Jackson, and A. Lande, Phys. Lett. 43B, 191 (1973).

[15] H. Crannell, Nucl. Instrum. Methods 71, 208 (1969).

[16] E. M. Riordan, Ph.D. thesis, MIT Laboratory for Nuclear Science Technical Report 94, 1973.

[17] R. P. Feynman, Phys. Rev. Lett. 23, 1415 (1969); J. D. Bjorken and E. A. Paschos, Phys. Rev. 185, 1975 (1969); E. D. Bloom and F. J. Gilman, Phys. Rev. Lett. 25, 1140 (1970).

[18] S. J. Bordsky and G. R. Farrar, Phys. Rev. Lett. 31, 1153 (1973).

[19] R. Blankenbecler and S. J. Brodsky, Phys. Rev. D 10, 2973 (1974).

[20] L. L. Frankfurt and M. I. Strikman, Phys. Lett. 69B, 93 (1977); Nucl. Phys. B148, 107 (1979); M. Chemtob, *ibid.* A336, 229 (1980).